PAPER

Computational and experimental investigation of plasma deflagration jets and detonation shocks in coaxial plasma accelerators

IOP Publishing Plasma Sources Science and Technology
Plasma Sources Sci. Technol. **27** (2018) 025016 (14pp) https://doi.org/10.1088/1361-6595/aaabec

Computational and experimental investigation of plasma deflagration jets and detonation shocks in coaxial plasma accelerators

Vivek Subramaniam[1,3], **Thomas C Underwood**[2], **Laxminarayan L Raja**[1] **and Mark A Cappelli**[2]

[1] Department of Aerospace Engineering and Engineering Mechanics, The University of Texas, Austin, TX, United States of America
[2] Department of Mechanical Engineering, Stanford University, CA, United States of America

E-mail: vivek91@utexas.edu

Received 21 September 2017, revised 2 December 2017
Accepted for publication 31 January 2018
Published 23 February 2018

Abstract

We present a magnetohydrodynamic (MHD) numerical simulation to study the physical mechanisms underlying plasma acceleration in a coaxial plasma gun. Coaxial plasma accelerators are known to exhibit two distinct modes of operation depending on the delay between gas loading and capacitor discharging. Shorter delays lead to a high velocity plasma deflagration jet and longer delays produce detonation shocks. During a single operational cycle that typically consists of two discharge events, the plasma acceleration exhibits a behavior characterized by a mode transition from deflagration to detonation. The first of the discharge events, a deflagration that occurs when the discharge expands into an initially evacuated domain, requires a modification of the standard MHD algorithm to account for rarefied regions of the simulation domain. The conventional approach of using a low background density gas to mimic the vacuum background results in the formation of an artificial shock, inconsistent with the physics of free expansion. To this end, we present a plasma-vacuum interface tracking framework with the objective of predicting a physically consistent free expansion, devoid of the spurious shock obtained with the low background density approach. The interface tracking formulation is integrated within the MHD framework to simulate the plasma deflagration and the second discharge event, a plasma detonation, formed due to its initiation in a background prefilled with gas remnant from the deflagration. The mode transition behavior obtained in the simulations is qualitatively compared to that observed in the experiments using high framing rate Schlieren videography. The deflagration mode is further investigated to understand the jet formation process and the axial velocities obtained are compared against experimentally obtained deflagration plasma front velocities. The simulations are also used to provide insight into the conditions responsible for the generation and sustenance of the magnetic pinch. The pinch width and number density distribution are compared to experimentally obtained data to calibrate the inlet boundary conditions used to set up the plasma acceleration problem.

Keywords: magnetohydrodynamics, plasma accelerators, mode transition

1. Introduction

Coaxial plasma accelerators [1, 2] have been used in a wide variety of applications such as space propulsion [3], materials

[3] Author to whom any correspondence should be addressed.

processing [4], neutron generation [5] and as a laboratory scale platform for studying astrophysical phenomena [6]. The hypervelocity plasma jet that emerges from the accelerator exhibits a large number density and a high degree of collimation [7, 8] making it attractive for studying plasma material interactions. Recent experiments carried out by Loebner *et al* on the Stanford plasma gun (SPG) facility [9] examine the material response to the impingement of these jets on target surfaces. The motivation here is to use these plasma jets to mimic the transient loading on the inner walls of nuclear fusion reactors during edge localized mode disruption events. Depending on the delay between the gas loading into the interelectrode volume and the discharging of the electrodes, the accelerator is known to exhibit two distinct modes of operation [10–14]. In the case where the electrodes are stood off to a high potential difference before introducing the gas, the accelerator operates in the 'deflagration' mode [11]. This mode is characterized by a vacuum expansion and the formation of a stationary and diffuse current conduction zone that continually processes the incoming neutral gas into a hypervelocity plasma jet [15]. The deflagration mode is efficient in generating high energy directed plasma jets since a large fraction of the input electromagnetic energy is converted into kinetic energy of the jet [7, 10]. This aspect of the deflagration mode is beneficial from the standpoint of studying material interactions since higher kinetic energies correspond to larger stagnation pressures upon impact. Operating the accelerator with longer delays between gas-loading and capacitor discharging results in the 'detonation' mode that is characterized by a sharp current conduction zone [13, 14]. Also referred to in the literature as the 'snowplow' mode [12], the plasma detonation exhibits a magnetohydrodynamic (MHD) shock that accumulates the prefill gas as it expands out of the accelerator. Owing to the conversion of the magnetic energy into undirected thermal energy in the shock, the detonation mode results in the generation of lower plate-stagnation pressures as compared to the deflagration mode. Several theories have been proposed to explain the mode transition behavior such as the MHD Rankine–Hugoniot theory by Cheng [11, 15] and the plasma resistivity theory by Woodall and Len [12].

There exists a strong connection between the stagnation conditions generated on the target surface and the acceleration physics that dictates the operation mode of the plasma gun. The objective of the current study is to employ a simulation based on the MHD governing equations to isolate and study different aspects of the acceleration physics in the SPG. The SPG experiments initiate the plasma discharge in the deflagration mode. However, since the net current through the gun exhibits a time-variation in the form of a damped sinusoidal pulse typical of a LRC circuit, the second half of the ringing cycle displays a detonation mode. Hence, the plasma acceleration over the entire sinusoidal pulse displays a behavior characterized by a mode transition [10]. The first part of this study is concerned with obtaining a qualitatively consistent prediction of the mode transition. The number density profiles from the simulations are compared with spatially resolved Schlieren images for different halves of the ringing cycle to ascertain the ability of the MHD modeling framework towards resolving the mode transition behavior. Due to the presence of an initially evacuated domain, simulating the plasma acceleration in the deflagration mode becomes a numerically challenging task. Namely, the MHD numerical model, a continuum based formulation, is invalid in vacuum and the near-vacuum rarefied regions of the jet. This issue is unique to the deflagration mode and has not been encountered in previous modeling studies [16–18] since the focus was on simulating the accelerator in the detonation mode. While there have been some efforts towards simulating the accelerator in the deflagration mode [19, 20], the vacuum background was dealt with by replacing it with a low background density gas. We demonstrate that this results in a jet profile that displays an artificial shock, inconsistent with the physics of free expansion. We present a novel plasma-vacuum interface tracking framework to obtain physically consistent profiles of high density plasma jets expanding into vacuum. The algorithm is employed to simulate a plasma deflagration and the axial velocities obtained are compared to the SPG measurements of the plasma emission front velocity. Lastly, data pertaining to the magnetic pinch [21–23] formed at the exit plane of the accelerator is compared with experimental measurements that characterize this region. The simulations are used to assess the validity of a hydrostatic pinch equilibrium model [24] that has been employed to obtain the magnetic field and pressure in this region.

The rest of this article is organized as follows. Section 2 outlines the framework used to simulate plasma accelerators. Section 2.1 deals with the governing equations and briefly describes the numerical methodology used to discretize and solve the MHD equations. Section 2.2 describes the SPG experimental setup followed by the boundary conditions in section 2.3 and initial conditions in section 2.4 used to set up the plasma acceleration simulation. Section 3 describes the results and the quantitative/qualitative comparisons with experiments starting from section 3.1 that deals with the mode transition, section 3.2 that describes the plasma deflagration jet and section 3.3 that investigates the pinch physics.

2. Methodology

2.1. Governing equations and numerical model

The MHD model is a 'single-fluid' description of a plasma with a single temperature local thermodynamic equilibrium (LTE) approximation used to define plasma composition and its thermodynamic properties [25]. The plasma is assumed to be quasineutral throughout the domain of interest [26]. The resistive MHD equations comprise two parts: a hydrodynamic part, that comprises the compressible Navier–Stokes equations with magnetic Lorentz force and Joule heating source terms [27] coupled with a Maxwell's equation component comprising the Faraday's and Ampere's laws. The entire system is closed by an equation of state and Ohm's law. The resistive MHD equations in conservative form [28] are

written as

$$\frac{\partial \rho}{\partial t} + \nabla \cdot (\rho \vec{V}) = 0, \tag{1}$$

$$\frac{\partial}{\partial t}(\rho \vec{V}) + \nabla \cdot (\rho \vec{V}\vec{V}) - \nabla\left(P + \frac{B_\theta^2}{2\mu_0}\right) = 0, \tag{2}$$

$$\frac{\partial}{\partial t}(\vec{B}) + \nabla \cdot (\vec{V}\vec{B} - \vec{V}\vec{B}) = -\nabla \times \left(\eta \frac{\nabla \times \vec{B}}{\mu_0}\right), \tag{3}$$

$$\frac{\partial}{\partial t}\left(\rho e_t + \frac{\vec{B}.\vec{B}}{2\mu_0}\right) + \nabla \cdot \left(\left(\rho e_t + \frac{\vec{B}.\vec{B}}{\mu_0} + P\right)\vec{V} - \frac{\vec{V} \cdot \vec{B}}{\mu_0}\vec{B}\right) = -\frac{1}{\mu_0}\nabla \cdot (\eta(\nabla \times \vec{B}) \times \vec{B}), \tag{4}$$

$$\nabla.\vec{B} = 0. \tag{5}$$

The large Reynold's number and fast plasma transient allow for the viscous and conductive heat transfer effects to be ignored. ρ, P, $\vec{V}$ and $\vec{B}$ represent the plasma density, pressure, velocity vector and vector magnetic induction respectively. Here μ_0 refers to the magnetic permeability of free space. All of the aforementioned quantities are represented in S.I units. The density (ρ) in kg m^{-3}, pressure (P) in N m^{-2}, velocity ($\vec{V}$) in m s^{-1} and magnetic field ($\vec{B}$) in Tesla (T). Additionally, η represents the plasma resistivity and e_t the specific total energy that is composed of the specific internal energy e and the specific kinetic energy $\frac{|\vec{V} \cdot \vec{V}|}{2}$, that is $e_t = e + \frac{|\vec{V} \cdot \vec{V}|}{2}$. The plasma resistivity η is a function of the plasma pressure and temperature. A tabulation based on the Spitzer resistivity model [29] is used to obtain the resistivity as a function of plasma temperature. The Spitzer resistivity model is given by

$$\eta = \frac{(5e - 5)\ln(\Lambda)}{T^{\frac{3}{2}}}. \tag{6}$$

The tabulation uses the hydrogen resistivity data from [30] to back out the parameter Λ. The real gas formulation with a variable gas constant is used to define the equation of state. This modified equation of state also gives the relationship between the internal energy density and the temperature. These are given by

$$e(T) = \frac{R(T)T}{\gamma - 1}, \tag{7}$$

$$P = \rho R(T)T. \tag{8}$$

The specific internal energy data from [30] is used to find the gas constant as a function of temperature. Equations (1)–(5) with the closure relations given by equations (6)–(8) provide a consistent description of the dense thermal plasma in coaxial plasma accelerators. Due to the coaxial geometry of the device, the MHD equations described above are solved in a cylindrical polar coordinate system. As a first approximation and in order to make the numerical simulation computationally feasible, the acceleration process is assumed to be axisymmetric, thereby transforming the 3D model into a 2D resistive MHD system that is the focus of this paper. The net radial current that passes between the electrodes is simulated by imposing an azimuthal magnetic field boundary condition at the boundary representing the inlet. An examination of the time-evolution equation for the magnetic induction vector indicates that a zero magnetic field initial condition coupled with a purely azimuthal field boundary condition generates a magnetic induction vector oriented along the azimuthal direction at all times. This ensures that the magnetic induction vector will always be given by $\vec{B}(t, r, z) = (0, B_\theta(t, r, z), 0)$, where t denotes time and r, z the radial and axial coordinates. Such a magnetic field topology trivially satisfies the zero divergence constraint, thereby ensuring that the magnetic field transport predicted by the numerical scheme is divergence free.

The governing equations described above are solved within a cell-centered finite volume framework on generalized unstructured grids. The convective flux reconstruction is performed using a local Lax–Friedrichs method [31] and the diffusive face fluxes are obtained using a gradient reconstruction technique (least-squares) followed by cell averaging [32]. The system ODE obtained after the spatial discretization is time integrated using the fully implicit backward Euler scheme. The algebraic system obtained as a result of the time discretization is solved using the Newton method. A detailed description of the numerical implementation can be found in [20].

2.2. Plasma gun geometry

A schematic of the plasma accelerator experiment carried out at the SPG facility [6] is shown in figure 1. The plasma gun is oriented in a rodded coaxial configuration with an internal diameter of 5 cm and a total axial extent of 23 cm. To provide a current conduction pathway, a set of stainless steel rod anodes are used in conjunction with a single copper cathode. The device is driven by charging a 56 μF capacitor bank to 3–10 kV and connecting it across the accelerator electrodes. Control of the initial operating mode of the device is afforded using a triggerable spark gap which allows the electrodes to be isolated from the charged capacitors until the experiment is ready to commence.

The plasma gun, at one end, is connected to a neutral gas plenum through a fast rise-rate, high mass-bit gas puff valve [33]. On the other end, it opens into a vacuum chamber, maintained at 10^{-7} Torr between successive firing events that encloses the entire gun, i.e. all regions downstream of the gas puff valve. The experiment is initiated by charging the capacitor bank to a desired voltage level and setting the appropriate spark gap delay for the accelerator. The gas puff valve is then opened, leading to the free expansion of neutral gas into the interelectrode volume. This neutral gas expansion continues until either sufficient gas pressure is present for breakdown to occur or until the spark gap switch connects the charged capacitor bank to the electrodes. As the gas expands and approaches the Paschen breakdown pressure from the lower pd side, rapid production of electrons takes place leading to the formation of a two-temperature plasma. The non-equilibrium plasma consists of high energy electrons and a low temperature background gas (~300 K). Owing to

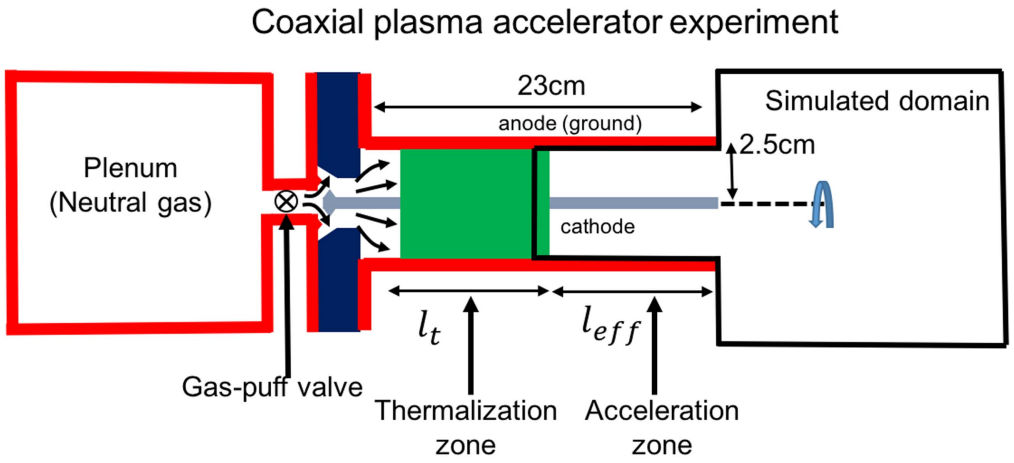

Figure 1. Schematic of experiment and illustration of the simulation domain. Adapted from [20], with the permission of AIP Publishing. The simulated domain (black boundary) includes the acceleration zone and the external plasma jet.

energy transfer mechanisms in the form of elastic and inelastic collisions, thermal equilibration between the electrons and the heavy species occurs in the vicinity of the inlet/breech end of the device [27]. The characteristic timescale of this equilibration process, under a Lagrangian transform performed using the free expansion velocity of the neutral gas, yields a length scale of equilibration. This is referred to in figure 1 as the thermalization zone (l_t).

To estimate the length scale over which neutral gas is transformed into conducting plasma, the time delay between the opening of the gas valve and the subsequent current flow from the capacitor banks was measured. By further assuming the gas is moving at its respective thermal velocity, a length scale of approximately 4 cm was estimated for the thickness of the thermalization zone for H_2. Much of this region can be attributed to the geometric design of the gas feed and more specifically, how much radial distance the neutral gas must traverse before simultaneously coming into contact with both the cathode and anodes. The determination of the thermalization length yields an effective length (l_{eff}) of the gun over which the plasma acceleration occurs (acceleration zone). This is the portion of the gun that can be modeled using the MHD formulation since the plasma in this region is in LTE between the heavy species and electrons, treated as a single fluid. Since the assumptions that go into experimentally determining the length of the thermalization zone have large uncertainties associated with it, in this paper, the thermalization length and consequently the acceleration zone length l_{eff} are treated as a modeling parameter.

2.3. Boundary conditions

The plasma acceleration process over an effective gun length l_{eff} is simulated by specifying the temperature, pressure and velocity of the thermalized plasma as an inflow boundary condition. The plasma temperature is estimated from the experimental measurements of Woodall and Len [14] to be around 1 eV and the pressure is taken to be the choked flow pressure corresponding to a stagnation chamber pressure of 2 atm to match the experimentally regulated gas valve pressures [6–10]. The velocity boundary condition is obtained from the neutral gas front velocity measurements carried out in the SPG facility, determined to be of the order of $1000\ \text{m s}^{-1}$ [15]. The electromagnetic boundary conditions involve specifying the total current discharged through the accelerator. Since the non-equilibrium plasma in the thermalization zone is expected to conduct much lower currents than the arc in the acceleration zone, we assume that the total current passes through the thermalized/acceleration zone. The SPG experiments measure the total current discharged though the device during a single operational cycle using a Pearson wideband current probe. Owing to current continuity, the total current passes through the cathode at all axial locations upstream of the thermalized/acceleration zone. Given the total current through the cathode, Ampere's law can be applied over a circular cross-section at the interface of the non-thermal and thermal plasma (at a distance l_t from the breech) to obtain a magnetic field boundary condition for the inlet boundary. This formulation ensures a consistency between the experimentally observed currents and the magnetic fields used in the simulations. A detailed derivation of the inlet boundary conditions can be found in [20]. A schematic of the simulation domain to study the plume formation is shown in figure 2 below.

2.4. Initial conditions

The initial conditions (ρ^{b}, v_r^{b}, v_z^{b}, B_θ^{b}, P^{b}) determine the operation mode of the accelerator. In the SPG experiments, the interelectrode volume is completely evacuated and the electrodes are stood off at a high potential before introducing the gas puff. This produces the so called 'deflagration' mode of gun operation, characterized by a diffuse current conduction region towards the breech [13] that continuously processes the neutral gas, producing a high velocity plasma jet. On the other hand, operating the gun in a pre-filled background generates the 'detonation' mode of operation, characterized by a sharp current conduction zone that traverses the length of the gun from the breech to the muzzle. The sharp conduction zone is a MHD shock formed due to the sudden

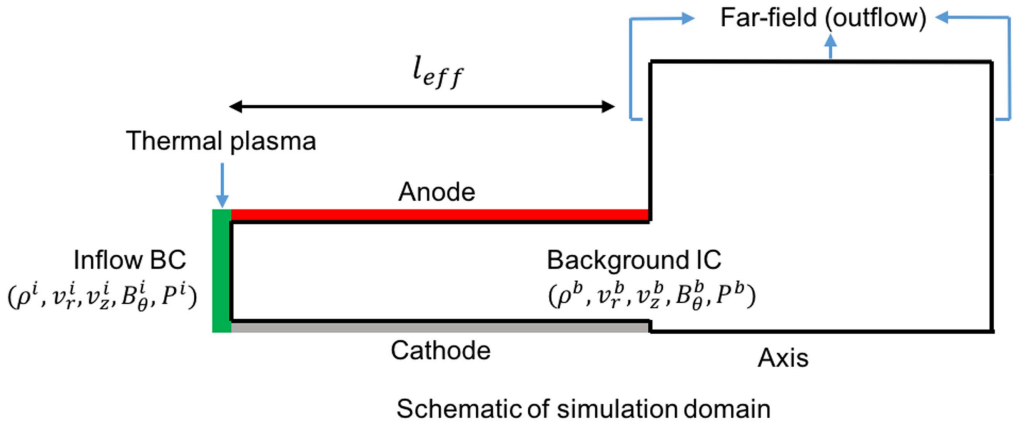

Figure 2. Schematic of the axisymmetric domain indicating the boundary conditions and initial conditions used to set up the plasma acceleration simulation.

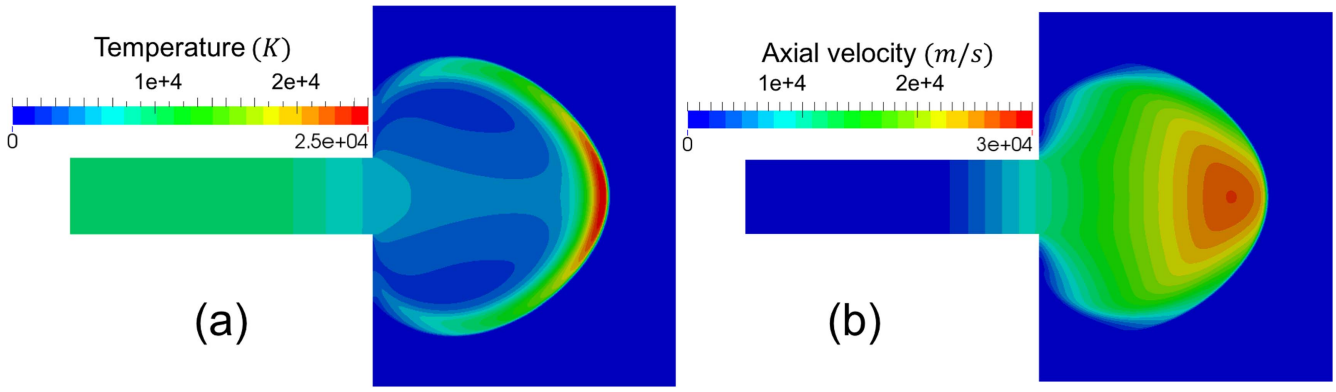

Figure 3. (a) Temperature and (b) axial velocity obtained using the low background density approach, 0.5 μs after discharge initiation, indicating an abrupt shock at the plasma-background (i.e. vacuum) interface.

compression of the prefill background gas by the Lorentz force in the arc. The numerical simulation of these distinct modes of gun operation relies heavily on the initial conditions that set up the acceleration process. Simulating the detonation mode is relatively straightforward since it requires the specification of the pressure and density of the prefill gas. The deflagration mode however poses a challenge from a modeling perspective since the continuum assumption, that underlies the MHD formulation, is invalid for the near vacuum conditions necessary for the formation of this mode. Modeling this mode in a physically consistent manner would require a hybrid continuum-particle approach where a continuum model is used in the high density regions and a particle model is employed in the more rarefied regions [34]. This approach however tends to be computationally expensive. In order to avoid this computational cost, prior modeling efforts [20, 27] have employed a fictitious low density background gas with densities $\rho_b \sim 10^{-7}$ kg m^{-3} and pressure $P_b \sim 1$ Pa. Using this initial condition, the MHD equations were solved through the entire simulation domain. The rationale behind this approach was the assumption that expansion of the high density plasma into the fictitious background would mimic free expansion into vacuum. This approach however does not generate a physically consistent characterization of the free expansion process. It can be seen in figure 3(a) that the plume generated by using a fictitious background exhibits a shock, as seen in the temperature profile, in the region where the plasma jet interacts with the background. The shock, caused by compression of the fictitious background, leads to an inhibited expansion of the plasma jet, as seen in the axial velocity contour in figure 3(b).

2.5. Plasma vacuum interface tracking algorithm

In order to overcome this issue, a plasma-vacuum interface tracking framework has been developed. Within this formulation, as opposed to a fictitious low density background, a zero density and zero pressure background is employed. Since the MHD governing equations are invalid in the vacuum containing regions of the simulation domain, the equations are solved on a subset of the simulation domain that contains a finite density plasma. Thus, as opposed to the treatment of the plasma-vacuum expansion as an initial value problem as carried out in the literature [20, 27], our proposed approach treats free expansion as a moving boundary value problem. The moving boundary that represents the plasma vacuum interface is consistently tracked as a part of the solution and the MHD equations are exclusively solved in the regions classified as containing a plasma. A classifier based on a density threshold is used to classify cells in the computational domain that contain plasma from those that represent vacuum.

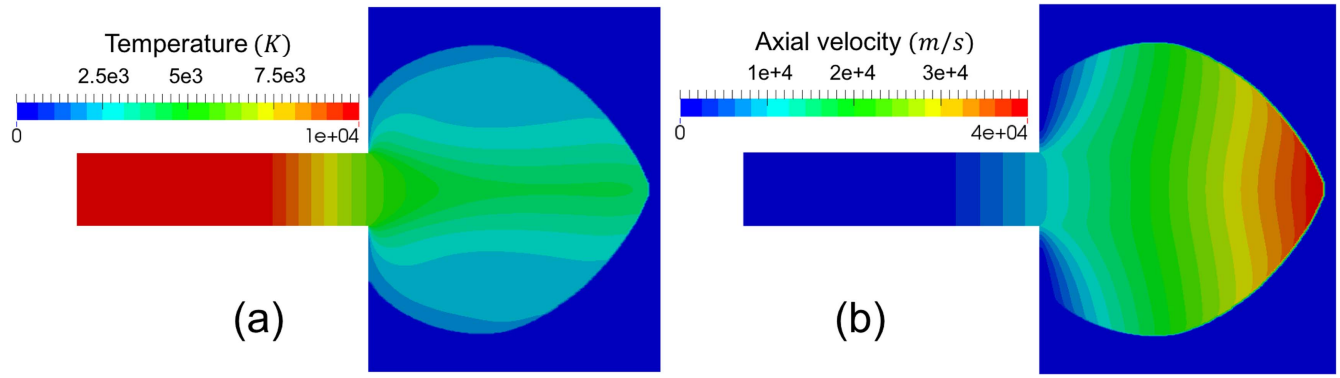

Figure 4. (a) Temperature and (b) axial velocity profiles obtained using the plasma-interface tracking approach, 0.5 μs after discharge initiation, indicating absence of a spurious shock at the plasma-vacuum interface.

In addition to tracking the plasma containing cells, the interface tracking algorithm also tracks the cells that contain vacuum and share a face with a plasma containing cell. These are referred to as interface cells. The plasma vacuum interface is identified as the faces in the computational mesh that divide plasma and interface cells. The algorithm proceeds as follows, first the plasma cells are updated by looping over the interior faces and computing the convective and resistive diffusion fluxes according to the formulation outlined in section 2.1. This computation, performed using the standard flux schemes i.e. local Lax–Friedrichs scheme for the convective flux and gradient reconstruction followed by averaging for the diffusive flux, is valid since both the adjacent cells contain a finite density plasma. This is followed computing the plasma-vacuum interface flux on the faces that contain a plasma cell on one side and an interface cell on another. The convective flux on this face accounts for the existence of vacuum in one of the adjacent cells and is computed based on the theoretical solution to a localized face-centered free expansion problem. This plasma-vacuum interface flux from the plasma cell to the interface cell leads to the filling up of the interface cell that initially contained vacuum, with a finite density plasma. As the density in these cells exceeds the threshold, they are classified as plasma cells and a new plasma-vacuum interface is identified. This process is repeated every time step to simulate the free expansion of plasma into the vacuum background. A crucial aspect to the algorithm is the choice of the density threshold. In the implementation of the plasma-vacuum interface tracking algorithm presented here, the density threshold is calibrated using the analytical solution to the 1D free expansion problem as a reference. The density threshold is varied till the plasma-vacuum interface location and tip velocity match the analytical solution at a given timestep. Once calibrated, the same density threshold is used to perform 2D simulations of plasma jets. The results obtained using this algorithm, as shown in the temperature contours in figure 4(a), indicate the absence of the spurious shock seen in figure 3(a) and a smooth decrease in temperature as one moves towards the tip of the plume. The axial velocity contours (figure 4(b)) indicate an expansion that is uninhibited by the background density, producing a jet with larger tip velocities as compared to the background density case (figure 3(b)).

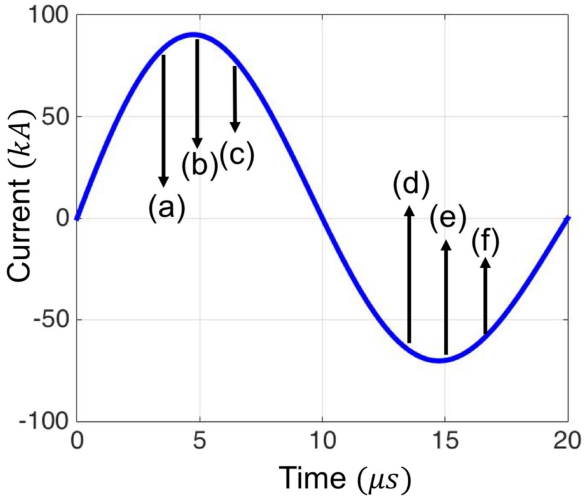

Figure 5. Damped sinusoid total current trace showing the times at which the number density time snapshots in figure 6 are obtained. Time shots (a)–(c) indicate the deflagration mode and (d)–(f) the detonation mode.

3. Results

3.1. Mode transition

The total current discharged through the accelerator during a single operational cycle exhibits the characteristics of a typical LRC circuit. The experimentally measured current trace, a damped sinusoid, is converted to a time-varying magnetic field boundary condition using Ampere's law as outlined in section 2.3. The total current discharged through the accelerator during a single operational cycle is shown in figure 5. In the first half of the ringing cycle, the accelerator operates in the deflagration mode, induced by evacuating the chamber and standing off the electrodes before triggering the gas-puff valve. In the simulations, this mode is mimicked by using the plasma-vacuum interface tracking framework to model the acceleration zone in figure 1.

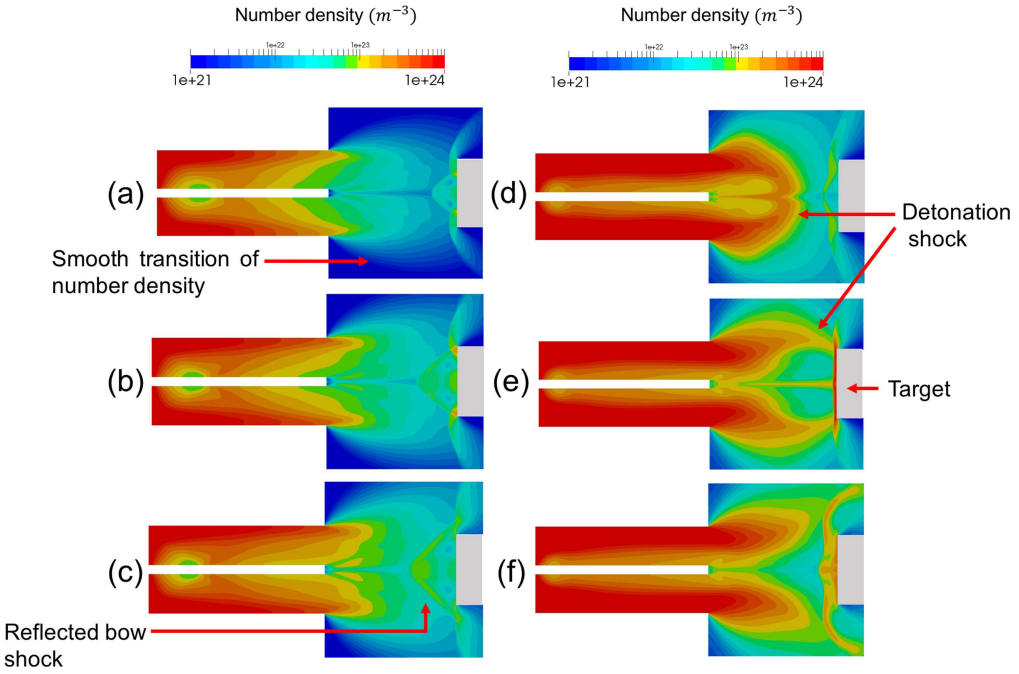

Figure 6. Number density contours during the deflagration mode (a)–(c) and detonation mode (d)–(f) operation. The deflagration mode shows a smooth transition to the background values, whereas the detonation mode exhibits a moving shock.

The number density contours at 3 different time instances 1 μs apart starting from 4 μs after the discharge initiation, are shown in figures 6(a)–(c). The location of these time snapshots on the total current trace in figure 5 is indicated by arrows and the corresponding figure number. In order to illustrate the effect of the mode transition on the plasma surface interactions, a target surface is placed at a distance of 7.5 cm from the accelerator exit.

The number density contours in the deflagration mode indicate a smooth transition in the number density profile from large values $\sim 10^{24}$ m^{-3} in core of the jet to smaller values $\sim 10^{21}$ m^{-3} in its peripheries. The impingement of the deflagration plasma plume on the target surface results in a reflected bow shock structure near the plate center and a normal shock towards the plate edge. The impinging plasma plume however, exhibits a monotonically decreasing number density in the regions preceding the shock. The spatial distribution of number density within the impacting jet influences the development of the shock structure at the target surface. The smooth number density variation within the deflagration jet results in a uniform bow shock growth rate upon impact with the target surface. Both the bow shock stand off distance and shock width uniformly increase across the deflagration transients shown in figures 6(a)–(c). The pinch formed at the gun exit plane exhibits a local increase in number density as seen in figure 6(c). This occurs due to a stationary turning shock formed at the gun exit plane, in order to maintain a purely axial flow orientation necessitated by the axisymmetric boundary condition. However, this localized shock is a stationary feature, the location of which is completely dictated by the geometry of the device.

The detonation mode operation indicated in figures 6(d)–(f) by time snapshots 1 μs apart staring 14 μs after discharge initiation displays different characteristic behavior. Due to the initiation of the discharge in a background that is prefilled with the remnant gas from the positive cycle discharge event, the detonation mode exhibits a strong moving shock with large number densities ($\sim 10^{23}$ m^{-3}). The shock travels down the length of the accelerator and can be seen to emerge from the gun exit at the 14 μs transient (figure 6(d)). Although the detonation shock dissipates in strength as it moves further and expands in the chamber, its presence results in a characteristically different plasma surface response as compared to the deflagration jet. The impact of the shock front with the target surface, as captured in the 15 μs transient (figure 6(e)), results in the formation of a thin normal shock. It is also seen in figure 6(e) that the normal shock on the target plate is part of a larger shock structure extending from the gun exit to the target

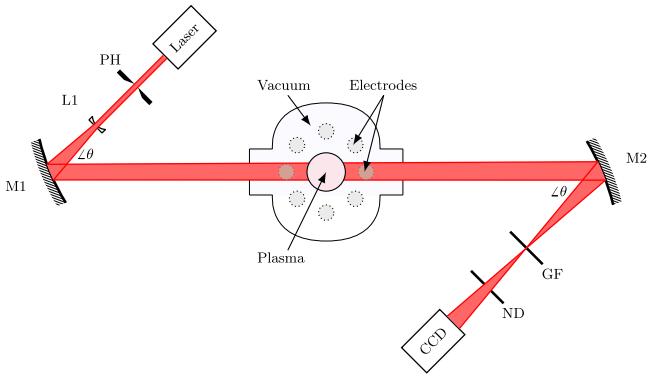

Figure 7. Experimental setup used to take high speed Schlieren images of the plasma flow. Relevant components include: laser-200 mW CW diode, PH: pinhole, L1: plano-convex lens, M1/M2: $f/4$. Schlieren mirrors, GF: neutral gradient filter, ND: neutral density filter, and CCD: Shimadzu HPV-X2 camera.

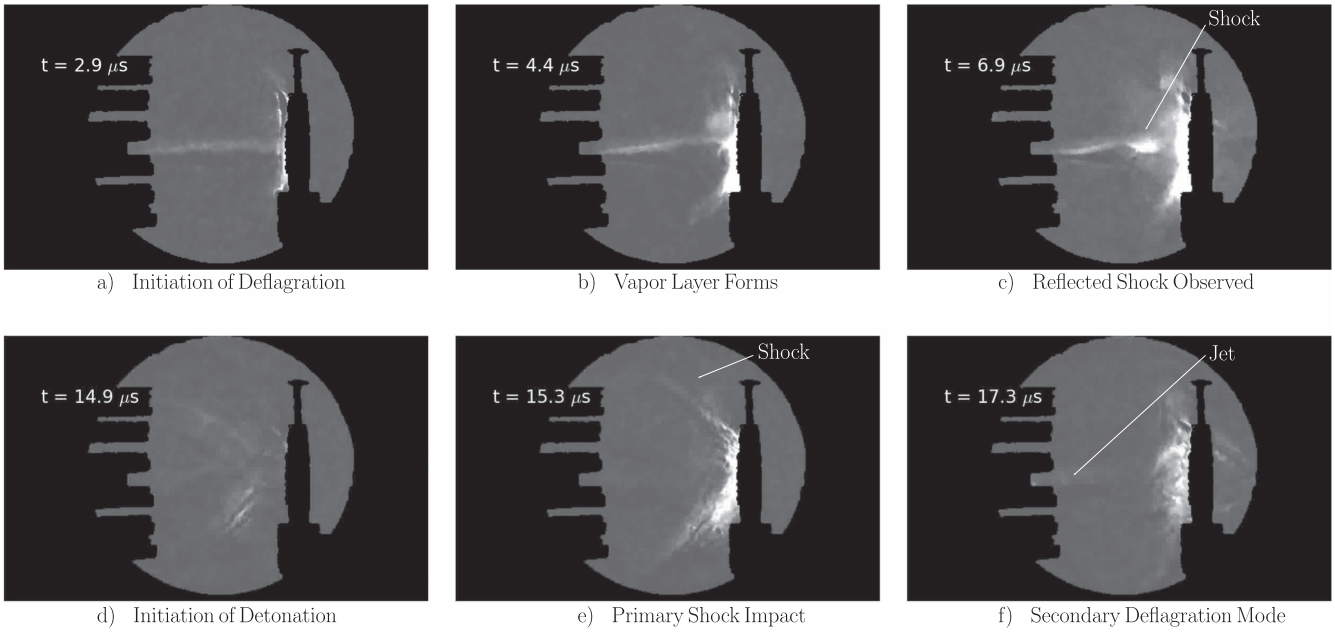

Figure 8. Schlieren images demonstrating a clear mode transition as predicted in accompanying numerical simulations. In these images, gradients in light correlate to gradients in the refractive index of the plasma.

plate. Following the detonation shock impact, the target surface normal shock exhibits an increase in the stand off distance and the radial extent to which it influences the detonation jet (figure 6(f)). Unlike the steadily growing bow shock structure formed on impact by the deflagration jet, the normal shock seen in the detonation mode exhibits a lower shock stand off distance and a highly unsteady radial growth rate. The lower stand off distance can be attributed to the higher free stream number densities and the presence of a moving shock front in the detonation jet. These conditions result in a significantly larger number density rise across the plate shock structure in the detonation mode as opposed to the deflagration mode. Since the shock stand-off distance is inversely proportional to the density ratio across the shock, the detonation mode plate shock exhibits a lower stand-off distance. The moving shock also leads to smaller front velocity ($\sim$40 km s^{-1}) as opposed to the large deflagration velocities ($\sim$120 km s^{-1}) observed in the first half of the ringing cycle. This is consistent with experimental observations [10] that indicate a significant difference in the front velocities between the two modes of operation. Since a significant portion of the electromagnetic energy goes into shock heating, the detonation mode velocities are observed to be 30%–50% of the deflagration velocity.

Schlieren refractometry was used to experimentally observe the distinct modes of operation and further validate the numerical simulations. Unlike emission, where the relationship between measured intensity and plasma state properties is a complex relationship of state variables, Schlieren offers the unique advantage of having a signal proportional to the gradient of plasma index of refraction. To allow such images, a standard z-configuration optical arrangement was employed, as detailed in figure 7. Optical aberrations of the system were minimized by using a small offset angle, θ, between the laser beam and mirrors in addition to large $f/\#$ mirrors. Due to the extreme self-emission of the plasma, a 200 mW laser was used in conjunction with a laser line filter to ensure that light collected on the CCD detector was dominated by the desired signal. To combat the inherent diffraction effects introduced when using a coherent back-light, a neutral gradient filter was used in place of the more traditional knife edge. Finally, to enable temporal resolution of sufficient precision to facilitate comparison with numerical simulations, a 10 million frames-per-second Shimadzu HPV-X2 camera was incorporated into the experimental setup.

Schlieren images of the resulting plasma flow at select times chosen to correspond with numerical simulations detailed in figure 6 are shown in figure 8. Unlike higher pressure applications of refractometry, given the negligible neutral gas pressure levels, the observed gradient in refractive index is dominated by the plasma density which facilitates comparison with MHD simulations. The profiles shown in figure 8 exhibit a diffuse emission zone in the first half discharge cycle consistent with the density profiles observed in the deflagration mode figures 6(a)–(c). The second half of the ringing cycle is characterized by a relatively sharp high gradient region that moves from the breech to the muzzle, consistent with the shock observed in the detonation mode operation figures 6(d)–(f). The dissipation of the high gradient region as it moves into the plume is also consistent with the dissipation of the shock towards the plume peripheries as seen in figure 6(e).

3.2. Deflagration velocity

Recent experiments carried out at the SPG facility determine the plasma deflagration velocity using a time of flight method by tracking the jet's leading edge [6]. The snapshots of the jet emission are used to identify a plasma-vacuum front using an edge tracking algorithm. The position of the jet leading edge

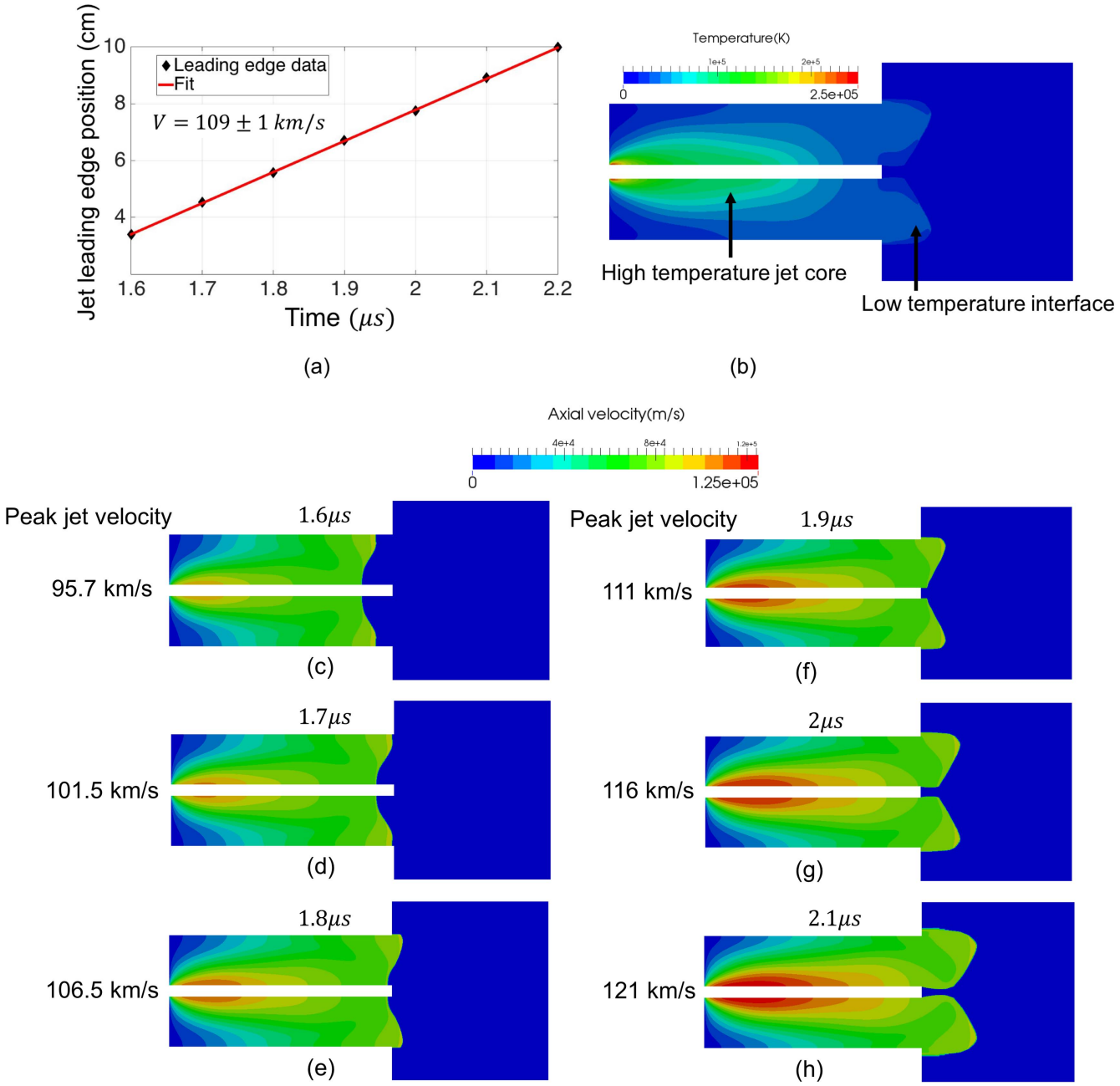

Figure 9. (a) Plasma-vacuum front position as a function of time obtained from the SPG experiments. (b) High-temperature jet core at a time instant of 2 μs obtained in the simulations. (c)–(h) Axial velocity time snapshots at various time-instances considered in (a) showing the maximum velocity obtained within the jet-core in each time snapshot.

is plotted as a function of time as shown in figure 9(a) and a jet velocity of 109 ± 1 km s^{-1} was found using the slope of the resulting line. Since the simulations yield an entire spatially resolved profile of the deflagration jet, axial velocities obtained in the jet are compared against the experimentally determined plasma front velocity. In the experiments, the jet velocity is obtained by performing the edge tracking on consecutive time shots starting at 1.6 μs, with an interval of 0.1 μs between successive shots. In order to perform the comparison, a series of six consecutive time shot outputs from the simulations, starting 1.6 μs after discharge initiation, are considered. The simulations also use a plasma-vacuum interface tracking framework as described in section 3.3. However, for the velocity comparison study, the velocity within the high temperature jet core (figure 9(b)), rather than the velocity of the plasma vacuum interface, is chosen to be compared against the experiments. This choice is dictated by the fact that the deflagration velocity within the high temperature jet core is determined by the Lorentz force dynamics as opposed to the plasma-vacuum interface velocity that is governed by free expansion physics. The resistive diffusion of the magnetic field within the jet core gives rise to high temperatures $\sim$20 eV. On the other hand, the negligibly low magnetic fields in the vicinity of the plasma-vacuum front result in comparatively lower temperatures ($\sim$0.5–1 eV) in this region. The disparity in the temperature between these

two regions is shown in figure 9(b). Due to the monotonic decay of density in the free expansion process, the plasma density is three orders of magnitude larger in the jet core as compared to the peripheral regions near the plasma-vacuum interface. Since the objective here is to characterize the dynamics within the magnetically accelerated high-density deflagration jet, the jet velocity within the high temperature jet core is compared against the experimentally obtained deflagration velocity.

The simulations indicate an increasing deflagration velocity as opposed to the constant jet velocity obtained in the experiments. This is consistent with the physics of electromagnetic acceleration since this is the portion of the ringing cycle where the input current and consequently the inlet magnetic field is increasing with time. This causes an increase in the Lorentz force and an associated increase in axial velocity as observed in figures 9(c)–(h). The peak axial velocities are close to the 109 km s^{-1} estimate obtained in the experiments with the peak being lower than this value in the first three time snapshots and greater than the value in the next three snapshots. In each of the time snapshots, the velocity in the high temperature region of the jet is closely distributed around the peak jet velocity, making the peak jet velocity a nominal measure for the plasma deflagration velocity.

3.3. Pinch characteristics

The SPG experiments [6] measure the time-integrated number density profile at the exit plane of the accelerator. The experimental pinch conditions are obtained using a combination of measured plasma properties in conjunction with a hydromagnetic equilibrium Bennett pinch model [6]. Experimental inputs to the pinch model are the spatially resolved plasma density which is quantified using Stark broadening of the $n = 3$ to $n = 2$ hydrogen Balmer-alpha (Hα) transition and discharge current. Using this information, the remaining critical features of the jet, namely magnetic field, temperature, and pressure are calculated. Specifically, a constant drift velocity model is applied to fully close the equilibrium pinch model. This amounts to assuming the current density to be proportional to the measured number density, $j = Cn(r)$. The proportionality constant, C, is determined from both $n(r)$ and I_p (the current flowing through the pinch) according to

$$C = \frac{I_p}{\int_0^{2\pi}\int_o^a n(r) r \, \mathrm{d}r\mathrm{d}\theta}, \tag{9}$$

where a is the radius of the pinch. Noting the form of the current density, the azimuthal B-field is determined via Ampere's Law,

$$B_\theta(r) = \frac{\mu_0}{r}\int_0^r j(r')r'\mathrm{d}r'. \tag{10}$$

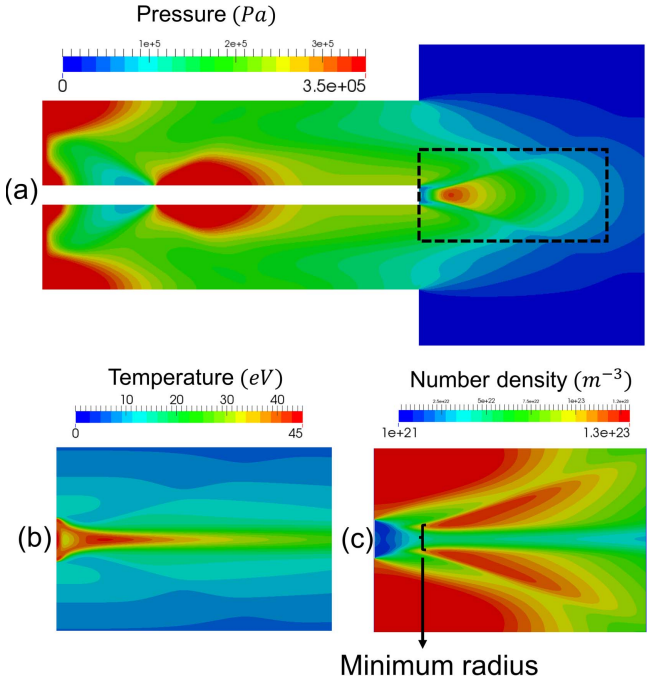

Figure 10. (a) Pressure profile contours indicating the pinch formed in the vicinity of the gun exit plane shown using a black-dashed box. (b) Enlarged view of the temperature distribution within the pinch region. (c) Enlarged view of density distribution within the pinch showing the minimum pinch radius identified using as the location where the variation in density occurs over the smallest radial distance.

In the absence of an applied axial field, the momentum equation yields the equilibrium profile for a radial pinch,

$$\frac{\mathrm{d}p}{\mathrm{d}r} = -\frac{B_\theta(r)}{\mu_0 r}\frac{\mathrm{d}}{\mathrm{d}r}[rB_\theta(r)] \tag{11}$$

which is solved to yield the pressure profile, $p(r)$. Finally combining this with the density profile and utilizing the ideal gas law, the temperature profile becomes,

$$T(r) = \frac{p(r)}{(1 + 1/Z)n(r)k_\mathrm{b}}, \tag{12}$$

where Z is the ionization state of the bulk plasma ions ($Z = 1$ for hydrogen). In this section, the profiles obtained using this model in combination with experimental measurements of $n(r)$ and the total discharge current are compared with the pinch data obtained from the simulations. The Schlieren images indicate a minimum pinch radius of 3.6 mm for the 9 kV shots. Since the experiments exclusively characterize the minimum pinch radius region, the first step in the comparison process is the identification of an equivalent region in the simulations. The pressure profile contours in the gun and the plume region, towards the end of the first positive-half cycle of the discharge current, are shown in figure 10(a). The pinch region in the vicinity of the exit plane is indicated using a black dashed line. An enlarged view exclusively of the pinch region is shown in figures 10(b) and (c) indicating the temperature and density contours. The experiments back out a minimum pinch radius from the Schlieren images, where the signal obtained is proportional to

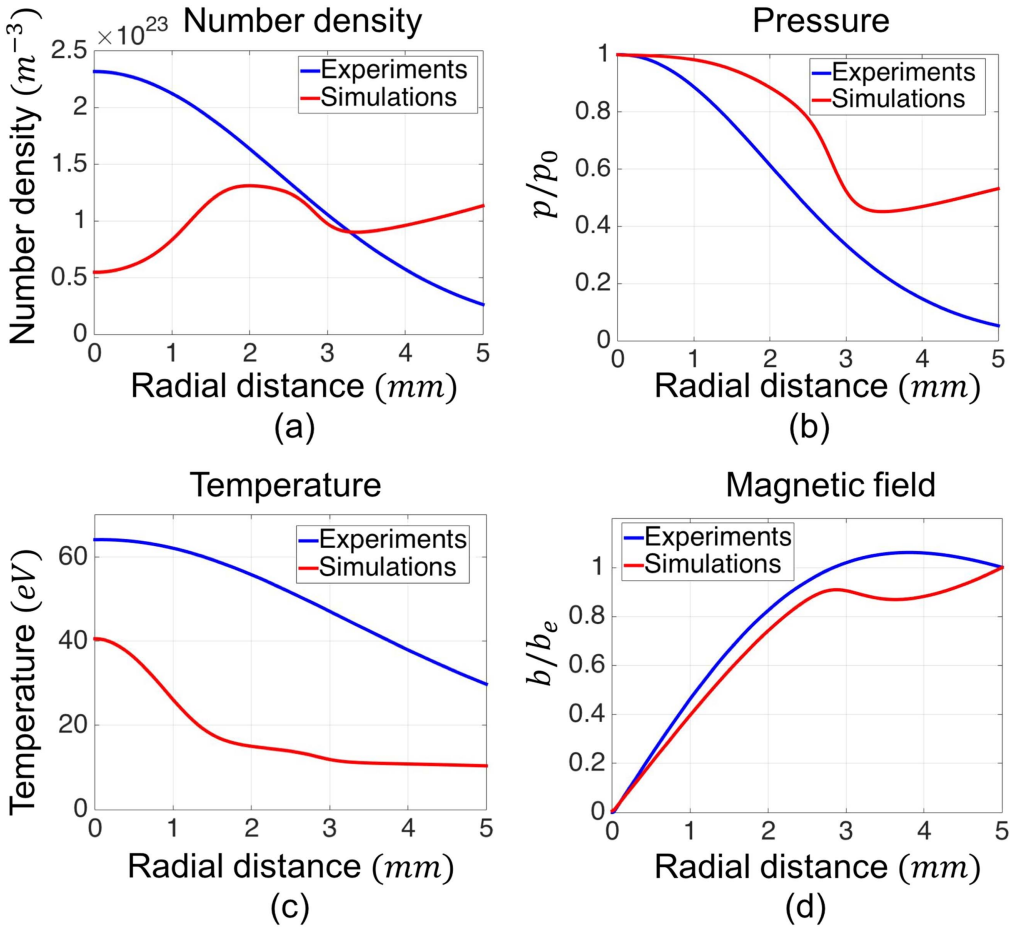

Figure 11. Comparison of simulation data at the minimum pinch radius with (a) number density obtained from the experiments and (b) pressure, (c) temperatur,e and (d) magnetic field inferred from equilibrium arguments.

the gradient of the index of refraction [6]. An equivalent minimum radius is obtained from the number density contours in figure 10(c), corresponding to the region in the pinch where the radial variation in the number density profile occurs over the smallest distance. The minimum radius region is shown in figure 10(c).

Once identified, the quantities of interest, namely the pressure, density, temperature and magnetic field within this region, are plotted as a function of radial distance from the axis, as shown in figure 11. Since the magnetic field and pressure data differ between the experiments and simulations (discussed below), a qualitative comparison of their distributions within the pinch is performed by dividing the pressure by the pressure at the pinch center and the magnetic field by the field at the pinch edge.

The line plots enable a quantitative estimation of the minimum pinch radius. The number density contours in figure 11(a) indicate a profile that exhibits a high density gradient region close to the axis with the density gradient going to zero at a radius of 3.2 mm. Following this region, the density smoothly increases with radial distance. Since the Schlieren signal is proportional to the refractive index gradient, the 3.2 mm mark where the density gradient goes to zero is identified as the boundary of the pinch. This gives a minimum pinch radius of 3.2 mm which is comparable to the 3.6 mm radius obtained in the experiments. Within this region, the pressure and magnetic field exhibit a quasi-equilibrium behavior with the gas-dynamic pressure (figure 11(b)) decreasing and magnetic field (figure 11(d)) increasing with radial distance from the axis. This is indicative of the momentum balance between the gas-dynamic pressure directed away from the axis and the inwardly directed magnetic pressure force.

In the experiments, the magnetic field distribution within the pinch is a derived quantity, obtained using the Bennet pinch model [6] (equations (9) and (10)). Here, the constant of proportionality between the plasma number density and pinch current density is derived by assuming that the net current through the accelerator passes through the minimum radius cross section of the pinch. Subsequently, the magnetic field is obtained from the current density distribution using Ampere's law (equation (10)). The MHD simulations on the other hand self-consistently compute the magnetic field within the pinch as the magnetic field is one of the conservative field variables in the governing equations system (section 2.1). In the MHD formulation, the current density is a derived variable, computed by taking gradients of the magnetic field in accordance with Ampere's law. The spatial distribution of current density through the simulation domain is predominantly dictated by the conductivity distribution, obtained using the Spitzer

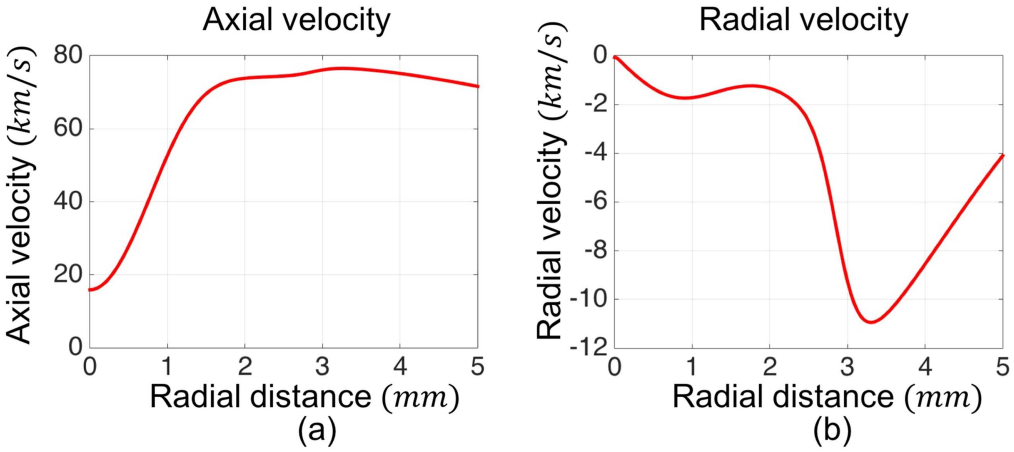

Figure 12. Simulation results for (a) axial velocity and (b) radial velocity at the minimum pinch radius as a function of radial distance from the axis.

conductivity formulation. The simulation results indicate an order of magnitude disparity in the magnetic field distribution through the pinch as compared to the experimentally derived field distribution. The value of the pinch edge magnetic field (b_e) in the simulations is found to be 0.25 T whereas the value obtained in the experiments is 1.7 T. This disparity exists despite the simulations predicting a number density distribution that is of the same order of magnitude as the experiments. One of the possible reasons contributing to the difference is the assumption of total current passage through the pinch, employed in the experiments to back out the magnetic field, that is not necessarily true in the simulations. Experiments carried out at the SPG facility using distributed dual-Rogowski coils indicate that, at times near the end of the first positive half-cycle, the discharge current is approximately equal to the axial current flowing through the tip of the cathode [14]. The time chosen to compare the experimentally derived pinch data with the simulation results corresponds to the end of the first positive-half cycle of the discharge current. Hence, it is assumed in the Bennett pinch model that, for the time at which the Stark broadening measurements were taken at the minimum pinch radius, the discharge current is equal to the axial current through the pinch. However, the simulations indicate that throughout the pinch formation event, the current distribution is associated with more than one region of high current densities. In addition to the pinch, the regions in the vicinity of the inlet/breech end of the accelerator also display large current densities. Hence, an order of magnitude lower current densities though the minimum pinch radius, as predicted by the simulations, are a contributing factor towards the order of magnitude difference in the pinch magnetic field between the simulations and experiments. This also necessitates the development of a higher fidelity conductivity model to preferentially bias the current conduction towards the high temperature regions in the vicinity of the pinch.

In the Bennett pinch model, the hydrostatic radial momentum equation is used to obtain the gas-dynamic pressure for a given magnetic field distribution within the pinch (equation (11)). The disparity in the magnetic field results in an equivalent order of magnitude difference in the gas-dynamic pressure between the simulations and the experiments. The pinch center pressure (p_0) is found to be 5 MPa in the experiments as opposed to 0.4 MPa in the simulations. The simulations also indicate that the pinch equilibrium is not strictly hydrostatic in nature. The velocity distribution within the pinch is shown in figure 12. The axial velocities (figure 12(a)) vary from 17 km s^{-1} near the axis to 80 km s^{-1} close to the pinch edge. The radial velocity profile (figure 12(b)) indicates the formation of a shock, which decreases the radial velocity from -11 km s^{-1} towards the pinch edge to around -50 m s^{-1} towards the axis. The shock is generated to ensure that the radial velocity goes to zero at the axis, a boundary condition imposed by the flow symmetry requirement at the axis. The influence of the radial shock on the pressure and magnetic field distribution is negligible since the dynamic pressure change across the shock, caused by the decrease in radial velocity, is small compared to the magnetic pressure/gas-dynamic pressure in this region. However, the radial shock significantly affects the number density distribution within the pinch. The shock is associated with a rise in number density in the post shock region, the maximum density observed at a radial location of 2 mm situated at the inner edge of the shock. As a result, although the experiments and simulations predict plasma densities in the pinch that are nominally of the same order of magnitude as shown in figure 11(a), the density distribution obtained from the simulations, as opposed to the experiments, indicates an off-axis density peak.

The plasma densities at the pinch display a high degree of sensitivity to the inlet boundary conditions used to set up the plasma acceleration. Initial efforts towards simulating plasma accelerators [20, 27] assumed an inlet temperature of $\sim$1 eV, a value that accounted for the gas-heating effects induced by high energy electrons. An inlet pressure of 1 atm was used to capture the choked flow conditions of a neutral gas bit expanding into an evacuated chamber from a plenum at a pressure of 2 atm. These initial conditions however, give pinch number densities that are one order of magnitude smaller than those obtained from the experiments. In order to obtain comparable pinch number densities, an inlet pressure

of 5 atm was employed for results outlined in figure 11. Since the ideal gas law (equation (8)) with a variable gas constant is used to specify the density given the pressure and temperature, the comparison study indicates that prior efforts towards simulating plasma accelerators obtained an order of magnitude lower density deflagrations as compared to the experiments. The high inlet pressure that results in comparable number densities at the pinch is indicative of a gas heating mechanism towards the inlet that simultaneously results in an increase in the pressure and temperature of the heavy species as they thermalize with the electrons.

4. Conclusion

A resistive MHD simulation was used to understand the physics associated with various aspects of the plasma acceleration process in the SPG experiment. The MHD simulation is able to predict a mode transition behavior between consecutive ringing cycles of the external circuit. This was verified to be consistent with the Schlieren imaging time snapshots observed in the experiments. The deflagration mode exhibited a smooth variation in number density profile from the core of the jet to its peripheries whereas the detonation mode was shown to produce a moving shock caused by the compression of the prefill gas. The numerical scheme was modified to predict the free expansion process, an integral part of the deflagration cycle. This was achieved by incorporating a plasma-vacuum interface tracking algorithm into the MHD numerical framework. It was shown that this approach resulted in a physically consistent prediction of the free expansion process as compared to background density based methods that predict an artificial shock at the plasma-background interface. Thus, as opposed to previous methods that approximated the deflagration as a weak detonation (low density prefill) the interface tracking algorithm treats deflagration using a modified numerical framework that accounts for the physics of free expansion. The plasma deflagration mode was further investigated to compare the axial velocities obtained within the high temperature core of the jet with the experimentally obtained emission front velocity. The plasma velocities within the jet core were found to match the experimentally obtained front velocities. The simulations predict the formation of a magnetic pinch at the exit plane of the accelerator. The minimum pinch radius obtained in the simulations was found to agree well with that measured in the experiments. It was found that the pinch exhibited a strong shock starting from the pinch edge and extending to half the pinch radius. Hence, although the simulations predicted pinch number densities that were of the same order of magnitude as the experiments, the radial shock resulted in an off-axis number density peak unlike the central peak obtained in the experiments. A large disparity in the experimentally derived pressure and magnetic field data from that obtained in the simulations was attributed to the existence of multiple regions of high current density. The large current densities towards the breech/inlet end of the device resulted in an order of magnitude lower pinch current and consequently lower magnetic field/gas-dynamic pressure within the pinch as compared to the experiments. This motivates the need for higher fidelity conductivity models to predict a more physically accurate current density distribution through the accelerator. The pinch number densities were found to be highly sensitive to the inlet plasma pressure. The increased inlet plasma pressure required to match the number densities at the pinch with the experiments indicates a simultaneous increase in gas pressure and temperature during the course of the plasma thermalization process. The MHD equations presented here (section 2.1) implicitly assume the existence of an equilibrium plasma throughout the simulation domain. Hence, accurately modeling of the deflagration process relies heavily on the inlet pressure and temperature conditions used to introduce a single-temperature equilibrium plasma into the simulation domain. This dependency necessitates the need for a self-consistent non-equilibrium model with finite-rate ionization/momentum-exchange kinetics, to capture the breakdown, two-temperature plasma formation and subsequent thermalization process as the plasma expands through the thermalization zone (figure 1). The non-equilibrium model development will be the subject of future work.

Acknowledgments

This research was supported through a grant from the Department of Energy, DOE Grant No. DE-NA0002922, through the NNSA Stewardship Science Academic Alliance Program (SSAP).

ORCID iDs

Vivek Subramaniam https://orcid.org/0000-0002-8909-3631

References

[1] Cheng D Y 1971 Application of a deflagration plasma gun as a space propulsion thruster *AIAA J.* **9** 1681–5
[2] Marshall J 1960 Performance of hydromagnetic plasma gun *Phys. Fluids* **3** 134–5
[3] Hoyt R P, Scheuer J T, Schoenberg K F, Gerwin R A, Moses R W and Henins I 1995 Magnetic nozzle design for coaxial plasma accelerators *IEEE Trans. Plasma Sci.* **23** 481–94
[4] Yan P, Hui P, Zhu W and Tan H 1998 An investigation of the pulsed plasma for deposition of thin film materials *Surf. Coat. Technol.* **102** 175–81
[5] Bernard A, Cloth P, Conrads H, Coudeville A, Gourlan G, Jolas A and Rager J P 1977 The dense plasma focus—a high intensity neutron source *Nucl. Instrum. Methods* **145** 191–218
[6] Underwood T C, Loebner K T and Cappelli M A 2017 A plasma deflagration accelerator as a platformfor laboratory astrophysics *High Energy Density Phys.* **23** 73–80
[7] Loebner K T, Wang B C, Poehlmann F R, Watanabe Y and Cappelli M A 2014 High-velocity neutral plasma jet formed by dense plasma deflagration *IEEE Trans. Plasma Sci.* **42** 2500–1

[8] Loebner K T, Underwood T C, Mouratidis T and Cappelli M A 2016 Radial magnetic compression in the expelled jet of a plasma deflagration accelerator *Appl. Phys. Lett.* **108** 094104
[9] Loebner K T, Underwood T C, Wang B C and Cappelli M A 2016 Damage morphologies in targets exposed to a new plasma deflagration accelerator for ELM simulation *IEEE Trans. Plasma Sci.* **44** 1534–40
[10] Loebner K T, Underwood T C and Cappelli M A 2015 Evidence of branching phenomena in current-driven ionization waves *Phys. Rev. Lett.* **115** 175001
[11] Cheng D Y 1970 Plasma deflagration and properties of a coaxial plasma deflagration gun *Nucl. Fusion* **10** 11
[12] Woodall D M and Len L K 1985 Observation of current sheath transition from snowplow to deflagration *J. Appl. Phys.* **57** 961–4
[13] Poehlmann F R, Gascon N and Cappelli M A 2007 The deflagration—detonation transition in gas-fed pulsed plasma accelerators *AIAA Joint Propulsion Conf., (Cincinnati, OH)* AIAA-2007-5263
[14] Poehlmann F R, Cappelli M A and Rieker G B 2010 Current distribution measurements inside an electromagnetic plasma gun operated in a gas-puff mode *Phys. Plasmas* **17** 123508
[15] Poehlmann F R 2010 Investigation of a plasma deflagration gun and magnetohydrodynamic Rankine–Hugoniot model to support a unifying theory for electromagnetic plasma guns *PhD Thesis* Dept. of Mechanical Engineering, Stanford University
[16] Sankaran K, Martinelli L, Jardin S C and Choueiri E Y 2002 A flux-limited numerical method for solving the MHD equations to simulate propulsive plasma flows *Int. J. Numer. Methods Eng.* **53** 1415–32
[17] Mikellides P G, Turchi P J and Roderick N F 2000 Applied-field magnetoplasmadynamic thrusters: I. Numerical simulations using the MACH2 code *J. Propulsion Power* **16** 887–93
[18] Witherspoon F D, Case A, Messer S J, Bomgardner R, Phillips M W, Brockington S and Elton R 2009 A contoured gap coaxial plasma gun with injected plasma armature *Rev. Sci. Instrum.* **80** 083506
[19] Sitaraman H and Raja L L 2014 Magneto-hydrodynamics simulation study of deflagration mode in co-axial plasma accelerators *Phys. Plasmas* **21** 012104
[20] Subramaniam V and Raja L L 2017 Magnetohydrodynamic simulation study of plasma jets and plasma-surface contact in coaxial plasma accelerators *Phys. Plasmas* **24** 062507
[21] Shumlak U, Nelson B A, Golingo R P, Jackson S L, Crawford E A and Den Hartog D J 2003 Sheared flow stabilization experiments in the ZaP flow Z pinch *Phys. Plasmas* **10** 1683–90
[22] Shumlak U and Hartman C W 1995 Sheared flow stabilization of the $m = 1$ kink mode in Z pinches *Phys. Rev. Lett.* **75** 3285
[23] Shumlak U, Golingo R P, Nelson B A and Den Hartog D J 2001 Evidence of stabilization in the Z-pinch *Phys. Rev. Lett.* **87** 205005
[24] Jackson S L 2010 Density characteristics of a sheared-flow Z-pinch *PhD Thesis* University of Washington
[25] Goldston R J and Rutherford P H 1995 *Introduction to Plasma Physics* (Boca Raton, FL: CRC Press)
[26] Inan U S and Gołkowski M 2010 *Principles of Plasma Physics for Engineers and Scientists* (Cambridge: Cambridge University Press)
[27] Sitaraman H 2013 Magneto-hydrodynamics simulation study of high density thermal plasmas in plasma acceleration devices *PhD Thesis* The University of Texas at Austin
[28] Bittencourt J A 2013 *Fundamentals of Plasma Physics* (New York: Springer)
[29] Spitzer L Jr and Harm R 1953 Transport phenomena in a completely ionized gas *Phys. Rev.* **89** 977–81
[30] Boulos M I, Fauchais P and Pfender E 2013 *Thermal Plasmas: Fundamentals and Applications* (New York: Springer)
[31] LeVeque R J 2002 *Finite Volume Methods for Hyperbolic Problems* vol 31 (Cambridge: Cambridge University Press)
[32] Haselbacher A and Blazek J 2000 Accurate and efficient discretization of Navier–Stokes equations on mixed grid *AIAA J.* **38** 2094–102
[33] Loebner K T, Underwood T C and Cappelli M A 2015 A fast rise-rate, adjustable-mass-bit gas puff valve for energetic pulsed plasma experiments *Rev. Sci. Instrum.* **86** 063503
[34] Roveda R, Goldstein D B and Varghese P L 2000 Hybrid Euler/direct simulation Monte Carlo calculation of unsteady slit flow *J. Spacecr. Rockets* **37** 753–60